*Nano Research* 2015, 8(12): 4061–4071
DOI 10.1007/s12274-015-0917-5
**Research Article**
ISSN 1998-0124
CN 11-5974/O4

# Effect of defects on photocatalytic activity of rutile $TiO_2$ nanorods

Zhao Zhao[1,2,3,4], Xiaoyan Zhang[1,3], Guoqiang Zhang[1,3], Zhenyu Liu[1], Dan Qu[1,3], Xiang Miao[1,3], Pingyun Feng[4] (✉), and Zaicheng Sun[1,2] (✉)

[1] *State Key Laboratory of Luminescence and Applications, Changchun Institute of Optics, Fine Mechanics and Physics, CAS.3888 East Nanhu Road, Changchun 130033, China*
[2] *Beijing Key Laboratory for Green Catalysis and Separation, Department of Chemistry and Chemical Engineering, Beijing University of Technology, Beijing 100124, China*
[3] *University of Chinese Academy of Sciences, No.19A Yuquan Road, Beijing 100049, China*
[4] *Department of Chemistry, University of California, Riverside, CA 92521, USA*

**Received:** 21 August 2015
**Revised:** 27 September 2015
**Accepted:** 29 September 2015



## KEYWORDS

$TiO_2$,
oxygen vacancies,
photocatalytic $H_2$ generation,
defects,
charge separation

## ABSTRACT

To further understand the effect of structural defects on the electrochemical and photocatalytic properties of $TiO_2$, two synthetic approaches based on hydrothermal synthesis and post-synthetic chemical reduction to achieve oxygen defect-implantation were developed herein. These approaches led to the formation of $TiO_2$ nanorods with uniformly distributed defects in either the bulk or on the surface, or the combination of both, in the formed $TiO_2$ nanorods (NRs). Both approaches utilize unique TiN nanoparticles as the reaction precursor. Electron microscopy and Brunauer-Emmett-Teller (BET) analyses indicate that all the studied samples exhibit similar morphology and similar specific surface areas. X-ray photoelectron spectroscopy (XPS) and electron paramagnetic resonance (EPR) data confirm the existence of oxygen defects ($V_O$). The photocatalytic properties of $TiO_2$ with different types of implanted $V_O$ were evaluated based on photocatalytic $H_2$ production. By optimizing the concentration of $V_O$ among the $TiO_2$ NRs subjected to different treatments, significantly higher photocatalytic activities than that of the stoichiometric $TiO_2$ NRs was achieved. The incident photon-to-current efficiency (IPCE) data indicate that the enhanced photocatalytic activity arises mainly from defect-assisted charge separation, which implies that photo-generated electrons or holes can be captured by $V_O$ and suppress the charge recombination process. The results show that the defective $TiO_2$ obtained by combining the two approaches exhibits the greatest photocatalytic activity enhancement among all the samples.

Address correspondence to Zaicheng Sun, sunzc@bjut.edu.cn; Pingyun Feng, pingyun.feng@ucr.edu

## 1 Introduction

Photocatalysis has attracted more and more interest because of its environmentally friendly nature and its potential applications in environmental remediation, solar energy conversion, and artificial photosynthesis [1–4]. Titanium dioxide ($TiO_2$) is one of the most widely studied inorganic semiconductor photocatalysts, owing to its high photocatalytic activity, photo- and chemical stability, non-toxicity, and ubiquity [5]. However, due to its large band gap (3.0 eV for rutile and 3.2 eV for anatase), $TiO_2$ only responds to UV radiation, which constitutes less than 5% of sunlight. In addition, the fast recombination rate of photo-generated electron–hole pairs and the slow hot carrier diffusion hinder the performance of $TiO_2$ and its practical application as an efficient photocatalytic material [6]. The intentional introduction of crystal defects (such as oxygen vacancies or $Ti^{3+}$) into $TiO_2$ crystal lattices has proved to be one of the most promising methods to address this problem, because defects can impact the functional properties of metal oxides, such as their electronic structure, charge transport, and catalytic performance [7–9]. Generally, oxygen vacancies ($V_O$) can be implanted in two ways: either on the surface by a physicochemical post-synthesis process or in the bulk by controlled reduction of crystallization. Recently, a few groups reported colored $TiO_2$ that possesses enhanced visible light photocatalytic activity and high quantum efficiency [10–15]. In most cases, the improved photocatalytic performance can be attributed to the $V_O$ implanted in the bulk or on the surface. Broad visible light absorption and improved charge separation efficiency were achieved by introducing a defect band below the conduction band of $TiO_2$ [5, 16, 17]. Li et al. introduced $V_O$ into metal oxides through thermal hydrogen treatment and indicated that $V_O$ may also serve as shallow donors and improve charge transfer at the interface between the metal oxide and electrolyte [18–20]. Our group also observed that there is an optimal oxygen vacancy concentration to achieve enhanced photocatalytic activity via hydrothermal treatment as well as post-synthesis chemical reduction [14, 18, 21]. However, few studies have investigated the effect of combined defects on the surface and in the bulk on the performance of $TiO_2$ nanocrystals.

In this work, TiN nanoparticles were selected as a reaction precursor. The present results show that when TiN nanoparticles are used as the precursor, the morphology of the synthesized materials can be maintained under different treatments so that the impact of the differences in the surface area and morphology of the synthesized materials on the photocatalytic activities can be minimized. In this study, four types of $TiO_2$ nanorods (NRs) are prepared: (1) stoichiometric nanorods, denoted as $TiO_2$; (2) nanorods with implanted oxygen vacancies obtained by surface reduction treatment ($V_{SO}$), denoted as S-$TiO_{2-x}$; (3) nanorods with bulk oxygen vacancies obtained by the hydrothermal crystallization process ($V_{BO}$), denoted as B-$TiO_{2-x}$, and (4) nanorods produced by a combination of the hydrothermal and surface reduction treatment processes ($V_{BSO}$), denoted as S-B-$TiO_{2-x}$. The effect of different oxygen vacancies introduced via the different synthetic approaches on the structural characteristics, electrochemical, and photocatalytic performance of $TiO_2$ are systematically studied. The present results show that by optimizing the defect concentrations, among all four types of $TiO_2$, the best $H_2$ evolution performance is achieved with the S-B-$TiO_{2-x}$ sample under both simulated solar light and visible light.

## 2 Experimental section

### 2.1 Chemicals and materials

TiN (99.8%, 25 nm), rutile $TiO_2$ (99.8%, 25 nm) nanoparticles, and $NaBH_4$ (98%) were purchased from Aladdin Reagent Company. Concentrated hydrochloric acid (37% by weight), concentrated nitric acid (65% by weight), ethanol (AR), and methanol (AR) were purchased from Beijing Chemical Reagent Company and used as-received without any further purification.

### 2.2 Preparation of rutile $TiO_2$ nanorods

In a typical reaction, 0.5 g TiN was digested in 30 mL of 4 M $HNO_3$ aqueous solution for 30 min. The dispersion was then transferred into a 50 mL Teflon-lined stainless steel autoclave. The sealed autoclave was heated to 180 ˚C in an electric oven and kept at 180 ˚C for 24 h.

Subsequently, the reaction autoclave was naturally cooled to room temperature. The final product was collected by filtration, washed with distilled water to neutral pH, and then dried at 70 ℃.

### 2.3 Preparation of rutile $TiO_2$ nanorods with $V_{BO}$ (B-$TiO_{2-x}$ NRs)

In a typical reaction, 0.5 g TiN was digested in 30 mL of 4 M HCl aqueous solution for 30 min. The dispersion was then transferred into a 50 mL Teflon-lined stainless steel autoclave. The sealed autoclave was heated to 180 ℃ in an electric oven and kept at 180 ℃ for 2 h. Subsequently, the reaction autoclave was naturally cooled to room temperature. The final product was collected by filtration, washed with distilled water to neutral pH, and then dried at 70 ℃. Other samples were prepared similarly with reaction times of 4, 6, 12, and 24 h, respectively.

### 2.4 Preparation of rutile $TiO_2$ nanorods with $V_{SO}$ (S-$TiO_{2-x}$ NRs)

At room temperature, 2 g of the $TiO_2$ NRs was mixed with 1.5 g of $NaBH_4$ and then thoroughly ground for 30 min. The mixture was transferred into a porcelain boat and placed in a tubular furnace, heated from room temperature to 300 ℃ under Ar atmosphere at a heating rate of 10 ℃/min, and then held at the designated temperature for 5–60 min. After naturally cooling to room temperature, the final product was simply washed with deionized water and ethanol several times to remove unreacted $NaBH_4$ and dried at 70 ℃.

### 2.5 Preparation of rutile $TiO_2$ nanorods with $V_{BSO}$ (S-B-$TiO_{2-x}$ NRs)

At room temperature, 2 g of B-$TiO_{2-x}$ NRs was mixed with 1.5 g of $NaBH_4$ and then ground thoroughly for 30 min. The mixture was transferred to a porcelain boat and placed in a tubular furnace, heated from room temperature to 300 ℃ under Ar atmosphere at a heating rate of 10 ℃/min, and then held at the designated temperature for 5–60 min. After naturally cooling to room temperature, the final product was simply washed with deionized water and ethanol several times to remove unreacted $NaBH_4$ and dried at 70 ℃.

### 2.6 Photocatalytic activity measurements

The photocatalytic activities of the samples were evaluated by photocatalytic $H_2$ generation. A photocatalyst sample (50 mg) loaded with 1 wt.% Pt was added to aqueous methanol (30 vol.%, 120 mL) in the cell and then magnetically stirred for the duration of the photocatalytic test. A 300 W Xe lamp (Beijing Perfectlight Technology Co., Ltd.) was used as the visible light source with an optical filter (UVIR-420, CE Aulight Inc.) to cut off the short wavelength component (<420 nm). An AM 1.5 simulated solar power system (CE Aulight Inc.) was used as a natural light irradiation source. The evolved gas was detected *in situ* by using an online gas chromatograph (GC-2014C, Shimadzu) equipped with a thermal conductivity detector (TCD).

### 2.7 Photoelectrochemical measurements

Photocurrents were measured by using an electrochemical analyzer (CHI 660C Instruments) in a standard three-electrode system with the as-prepared powders coated on F-doped $SnO_2$-coated glass (FTO glass) as the working electrode, a platinum minigrid electrode as the counter electrode, and a saturated calomel electrode (SCE) as the reference electrode. A 1.0 M NaOH aqueous solution was used as the electrolyte. A solar simulator (AM1.5) with a power of 100 mW/cm$^2$ was used as the illumination source.

### 2.8 Characterizations

X-ray diffraction (XRD) patterns of the crystalline samples were recorded by using an X-ray diffractometer (Bruker AXS D8 Focus), with Cu-K$\alpha$ radiation ($\lambda$ = 1.54056 Å). Transmission electron microscope (TEM) images were acquired by using an FEI Tecnai G2 instrument operated at 200 kV. Scanning electron microscope (SEM) images were acquired on a JEOL JSM 4800F instrument. UV-Vis absorption spectra were recorded on a UV-3600 UV-Vis-NIR scanning spectrophotometer (Shimadzu). X-ray photoelectron spectra were acquired on a Thermo Scientific ESCALAB 250 Multitechnique Surface Analysis instrument. Electron paramagnetic resonance (EPR) spectra were recorded at 100 K on a Bruker A-200 EPR spectrometer. The Brunauer-Emmett-Teller (BET) specific surface

area was measured using a Micromeritics ASAP 2010 system.

## 3 Results and discussion

Figure 1(a) shows a schematic of the route used to prepare $TiO_2$, $TiO_2$ with bulk defects (B-$TiO_{2-x}$), $TiO_2$ with surface defects (S-$TiO_{2-x}$), and $TiO_2$ with both bulk and surface defects (S-B-$TiO_{2-x}$). All the prepared samples have nanorod morphology. Firstly, two types of $TiO_2$ NRs, stoichiometric and non-stoichiometric, with similar morphology were prepared from the TiN precursor. The stoichiometric $TiO_2$ NRs (white powder) were obtained from the $HNO_3$ reaction media (Fig. S1 in the Electronic Material Supplementary (ESM)). During this process, the $V_O$ cannot be maintained because of the strong oxidizing ability of $HNO_3$. Non-stoichiometric B-$TiO_{2-x}$ NRs (blue powder) were prepared in HCl aqueous solution, where the $V_O$ (or $Ti^{3+}$) were uniformly dispersed in the bulk phase [22]. The sample color gradually changed from dark blue to light blue (Fig. S2 in the ESM) with an increase in the hydrothermal treatment time from 2 to 24 h. The XRD results (Fig. S3 in the ESM) indicate that the characteristic diffraction peaks of TiN gradually decreased and disappeared after 4 h of reaction time. When the hydrothermal reaction time exceeded 6 h, rutile $TiO_2$ was the only product. This observation indicates that TiN is gradually decomposed and oxidized during the reaction, which is consistent with the disappearance of the peak in the N 1s X-ray photoelectron spectroscopy (XPS) spectrum (Fig. S4 in the ESM). The rutile $TiO_2$ and B-$TiO_{2-x}$ nanorods were further treated with solid $NaBH_4$ at 300 ℃ for different times, thereby yielding S-$TiO_{2-x}$ and S-B-$TiO_{2-x}$ with variable oxygen vacancy concentrations [21]. The color of the samples gradually deepened (Figs. S5 and S6 in the ESM) with an increase of the reduction time. Figure 1(b) and Fig. S7 in the ESM show typical SEM images of the as-synthesized samples. All four types of samples have similar morphologies comprising tetragonal crystals with a pyramid-like end and lengths and widths of ~200 and ~20 nm, respectively. The shape and morphology were not changed after the chemical reduction treatments based on SEM analysis. This was further confirmed by the $N_2$ adsorption experiments

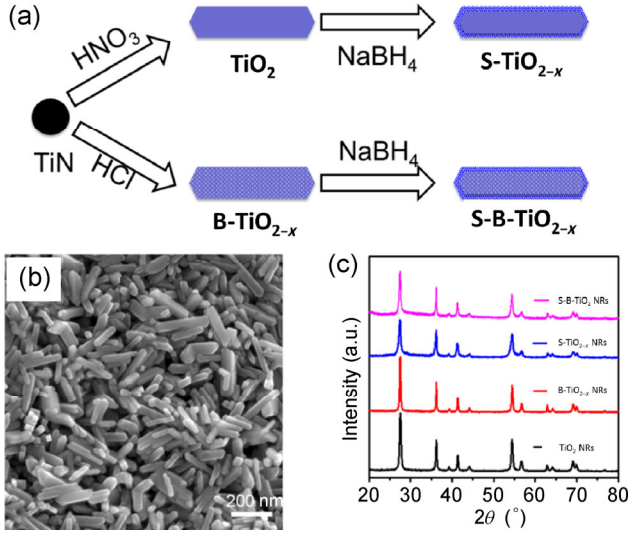


**Figure 1** (a) Strategies for synthesis of $TiO_2$ nanorods: $TiO_2$ with bulk oxygen vacancy (B-$TiO_{2-x}$), $TiO_2$ from surface reduction treatment (S-$TiO_{2-x}$), and $TiO_2$ from combination of two processes (S-B-$TiO_{2-x}$). (b) Typical scanning electron microscopy images of S-B-$TiO_{2-x}$, (c) XRD patterns of $TiO_2$, B-$TiO_{2-x}$, S-$TiO_{2-x}$, and S-B-$TiO_{2-x}$.

(Fig. S8 in the ESM). The BET surface area of the $TiO_2$ NRs, B-$TiO_{2-x}$ NRs, S-$TiO_{2-x}$ NRs, and S-B-$TiO_{2-x}$ NRs were 13.7, 19.6, 14.1, and 16.4 $m^2/g$, respectively. The powder X-ray diffraction patterns of all as-prepared samples were indexed in accordance with the rutile phase (Fig. 1(c)).

TEM images of the as-prepared $TiO_2$ NRs are shown in Fig. 2. The TEM images further confirm that the morphology of all samples remained visibly unchanged before and after the reduction treatment (inset: low-magnification TEM images). The high resolution TEM (HR-TEM) image shows a well-ordered lattice structure and clear 0.32 nm lattice fringes, corresponding to the fringe spacing between the (110) lattice planes of rutile $TiO_2$. The measured angle between the edges of the prismatic and pyramidal facets is 135° (Fig. 2(b)), which closely matches the theoretical angle between the (110) and (111) planes. Based on the above results, we can propose that the rutile $TiO_2$ NRs consist of a (110) tetragonal prism and a (111) tetragonal bipyramid, with preferentially developed (110) prismatic faces, and the elongated crystals are parallel to the *c*-axis. These features are similar to those of previously reported bulk $Ti^{3+}$-doped $TiO_2$ with active facets [23]. The stoichiometric $TiO_2$ NRs and the B-$TiO_{2-x}$ NRs (Figs. 2(a) and 2(b)) both have similar morphology.

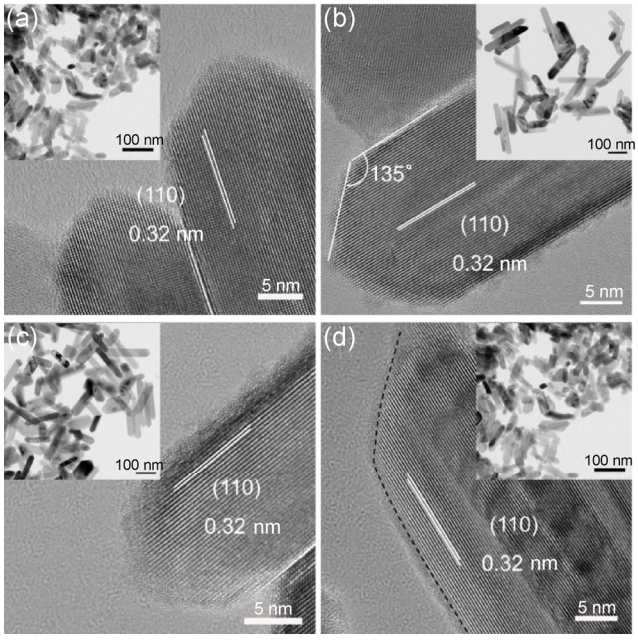


**Figure 2** HR-TEM images of $TiO_2$ (a), B-$TiO_{2-x}$ (b), S-$TiO_{2-x}$ (c), and S-B-$TiO_{2-x}$ (d). The insets are corresponding low magnification TEM images.

The HR-TEM images show that a disordered layer is formed after the chemical reduction treatment. Figures 2(c) and 2(d) show the HR-TEM images of the S-$TiO_{2-x}$ NRs and S-B-$TiO_{2-x}$ NRs after the chemical reduction treatment, which indicate a highly crystalline core with a clear, disordered shell of 1–2 nm [11, 24, 25]. The longer surface reduction treatment time (Fig. S9 in the ESM) results in increased crystalline lattice deformation and a thicker amorphous layer [26].

It is well known that the introduction of oxygen vacancies into $TiO_2$ can change white $TiO_2$ into a blue or black material (as shown in Figs. S3, S5, and S6), the color variation indicates enhanced visible light absorption by defective $TiO_2$ [27]. The diffuse reflectance UV-Vis spectra of different defective $TiO_2$ nanorods formed by using different reaction times are shown in Fig. 3. The absorption band edge near 400 nm corresponds to the intrinsic optical absorption band-edge of rutile $TiO_2$. Compared with white $TiO_2$ nanorods, the surface-implanted oxygen vacancy S-$TiO_{2-x}$ nanorods and bulk-oxygen vacancy B-$TiO_{2-x}$ nanorods exhibit significant absorption in the visible and near infrared ranges, which could contribute to the photocatalytic activity in the visible light range [28]. With prolonged reaction time, the intensity of this absorption band

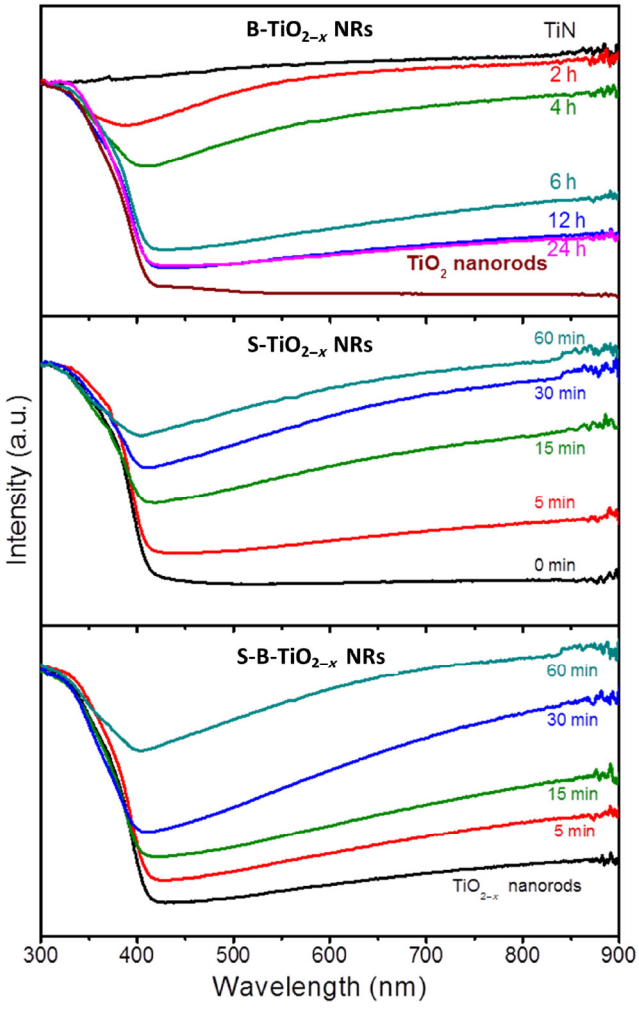


**Figure 3** Diffuse reflectance UV-Vis spectra of (a) B-$TiO_{2-x}$ nanorods prepared with different reaction times (2–24 h); (b) S-$TiO_{2-x}$ nanorods reduced for different times (5–60 min); (c) S-B-$TiO_{2-x}$ nanorods reduced for different times (5–60 min).

gradually decreased and the color of $TiO_2$ also changed to light blue (Fig. S2 in the ESM). These observations indicated that the oxygen vacancies or $Ti^{3+}$ concentrations could be tuned by changing the reaction time [14]. The electron paramagnetic resonance spectra (Fig. S10 in the ESM) showed a decrease in the intensity of the peaks with an increase of the reaction time, which further supports the aforementioned results. In addition, the samples prepared with reaction times of less than 4 h have higher absorption in the visible region due to the partial existence of residual TiN, which agrees with the XRD (Fig. S3 in the ESM) data. Figures 3(b) and 3(c) show the UV-Vis spectra of the samples treated with $NaBH_4$ at 300 °C for different

time periods. The results show significantly enhanced absorption from ~400 nm into the near-infrared region with increased reaction time. Again, the results can be correlated to the increased oxygen vacancies on the surface of the nanorods [14]. The improved optical absorption could contribute positively to the photocatalytic activity of the materials [29].

The valence state and composition of the samples were investigated by XPS (Fig. 4(a)). For the pristine stoichiometric $TiO_2$ NRs, a strong peak at 458.4 eV and a weak peak at 464.1 eV were apparent in the high resolution XPS spectrum, which can be attributed to Ti 2p 3/2 and Ti 2p 1/2. These are characteristic peaks of the $Ti^{4+}$-O bonds in $TiO_2$ as reported [30]. In the case of the B-$TiO_{2-x}$ NRs, the Ti 2p peaks shift to low binding energies of 458.0 and 463.8 eV, respectively. These shifts indicate the formation of $Ti^{3+}$ or oxygen vacancies in the nanocrystals [31]. In the case of the S-$TiO_{2-x}$ NRs and S-B-$TiO_{2-x}$ NRs, after the chemical reduction treatment, these peaks are further shifted to 457.7 and 463.5 eV, respectively. These results may indicate an increase in the surface defect species. However, with increasing chemical reduction treatment time, the characteristic Ti peaks shift back (Fig. S11 in the ESM) and the $Ti^{2+}$ peaks of TiO appear at 456.2 ($Ti^{2+}$ 2p 3/2), 458.2, and 459.7 eV ($Ti^{2+}$ 2p 1/2). These results may indicate that the increased concentration of oxygen vacancies or the existence of lower valence Ti species like $Ti^{2+}$ in the disordered layer lead to a decrease of the $Ti^{3+}$ species [14, 32].

EPR spectra recorded at 100 K were used to verify the presence of $Ti^{3+}$ and single electron trapped oxygen vacancies in the as-prepared samples. Not surprisingly, as shown in Fig. 4(b), no signals were detected for the pristine stoichiometric $TiO_2$ NRs. On the other hand, all of the $TiO_2$ NRs with defects showed unambiguously intense EPR signals. In the case of the B-$TiO_{2-x}$ NR sample, only a prominent signal at $g$ = 1.96 was detected, which could be attributed to $Ti^{3+}$ species present in the bulk of the material [15, 33]. In this case, oxygen vacancies generated on the surface of $TiO_2$ tend to be oxidized in air atmosphere. The structure on the surface may act as a passivation layer to protect the bulk oxygen vacancies from further oxidation [34, 35]. The intensity of the EPR signal of the B-$TiO_{2-x}$ NRs decreased with treatment times ranging from 4 to

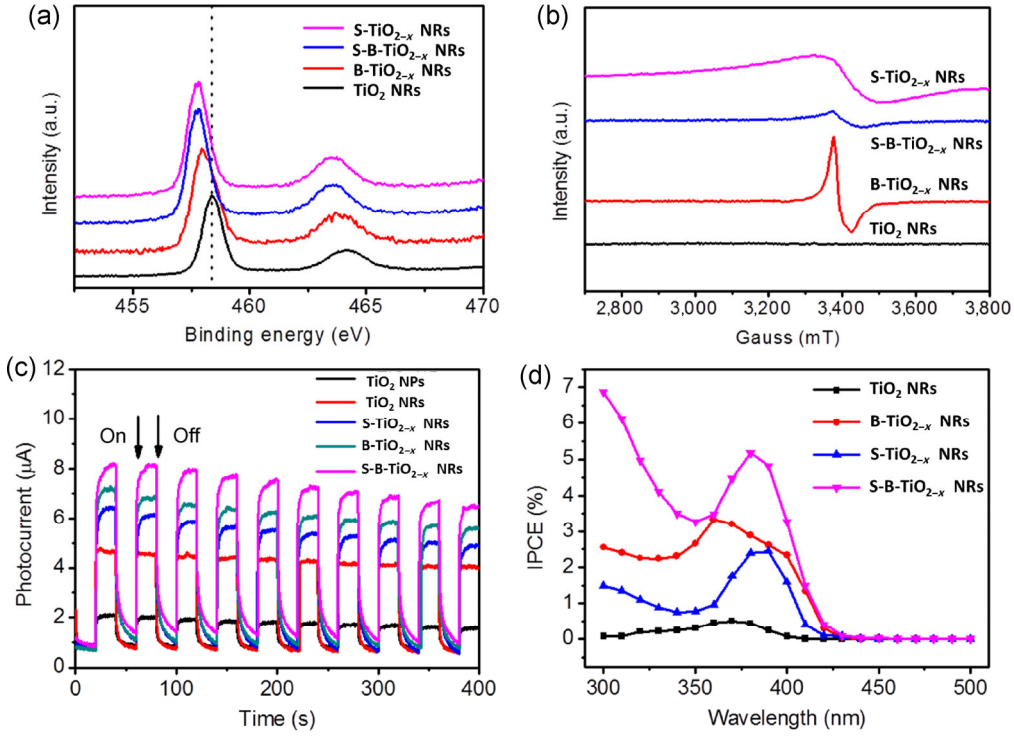


**Figure 4** (a) Ti 2p XPS spectra, (b) EPR spectra, (c) transient photocurrent responses, (d) IPCE at an applied potential of 0.3 V versus Ag/AgCl for $TiO_2$ nanorods and $TiO_2$ nanorods with different kinds of $V_O$. The electrolyte was 1 M aqueous KOH.

24 h (Fig. S12(a) in the ESM), indicating that the $Ti^{3+}$ in the bulk of the sample undergoes slow oxidation with prolonged reaction time. Both the color (Fig. S2 in the ESM) and photo-absorption (Fig. 3(a) in the ESM) of the samples reflect this change. The concentration of $Ti^{3+}$ was determined by numerical double integration of the EPR spectra and comparison with the spectrum of a frozen aqueous solution of $Cu^{2+}$. The concentration of $Ti^{3+}$ in the B-$TiO_{2-x}$ NRs prepared by hydrothermal reaction for 6 h was estimated to be 5.15 μmol/g, with an absolute accuracy of about 20% [36]. The concentration of $Ti^{3+}$ decreased to 3.05 μmol/g for the B-$TiO_{2-x}$ sample prepared over 24 h. In the case of the S-$TiO_{2-x}$ and S-B-$TiO_{2-x}$ NR samples, the disordered shell structure formed on the surface via chemical reduction may stabilize defects against air oxidation, and the surface oxygen vacancies may be able to trap electrons ($O_2^-$) from air [37, 38]. Both factors could contribute to the broad EPR signals observed for the S-$TiO_{2-x}$ and S-B-$TiO_{2-x}$ NRs samples [39, 40]. In addition, oxygen vacancies and other lower valence Ti species formed on the disordered surface of the samples may act as heterogeneities, which could result in the anomalous near-isotropic shape [41]. Broadened and more intense EPR signals were observed with longer reduction time, as shown in Fig. S12(b) (in the ESM), indicating that the concentration of oxygen vacancies in the samples increased with increasing reduction reaction time.

In order to investigate the effect of different defects on the photoelectrochemical properties, $TiO_2$ NP, $TiO_2$ NR, B-$TiO_{2-x}$ NR (6 h), S-$TiO_{2-x}$ NR (15 min), and S-B-$TiO_{2-x}$ NR (5 min) films were prepared by the electrophoretic deposition method. Generally, to increase the interconnection between the deposited films and the substrates and obtain better photocurrent, deposited films are subjected to $TiCl_4$ treatment and high temperature calcination [42]. However, in order to preserve the oxygen vacancy distribution in the samples, the electrochemical properties of the films were measured directly without further treatment herein. A set of photocurrent spectra of these films was recorded in the dark and under illumination from an AM 1.5 solar spectrum simulator with chopped linear-sweeps, as shown in Fig. 4(c). All the $TiO_2$ NRs with defects showed significantly enhanced performance in comparison with the pristine stoichiometric $TiO_2$ photoanodes. Under the same measurement conditions, the sample with oxygen vacancies implanted by the combination of two processes (S-B-$TiO_{2-x}$ NRs) showed the highest electrochemical performance among all the samples. The photocurrent increased from 4.3 μA for the $TiO_2$ NRs to 8.2 μA for the S-B-$TiO_{2-x}$ NRs. The higher photocurrents of the B-$TiO_{2-x}$ NRs, S-$TiO_{2-x}$ NRs, and S-B-$TiO_{2-x}$ NRs relative to that of pristine $TiO_2$ are an indication of more efficient charge separation and transport in the samples with oxygen defects.

In order to investigate the interplay between the photo-absorption and the photocatalytic activity, the incident photon-to-current conversion efficiencies (IPCEs) were measured at 0.3 V versus Ag/AgCl (Fig. 4(d)). In comparison with the pristine $TiO_2$ NRs, both the bulk-defective $TiO_{2-x}$ NRs and the surface-reduced $TiO_2$ NRs showed greatly enhanced IPCEs over the entire UV region. Moreover, the S-B-$TiO_{2-x}$ NR sample prepared by the two-step reduction process exhibited the highest conversion efficiency over the entire UV region. All the samples have an adsorption edge around 420 nm, which is consistent with the intrinsic optical absorption band-edge of rutile $TiO_2$ shown in Fig. 3. However, only low photoactivity in the visible light region was observed for the three nonstoichiometric $TiO_2$ samples and the IPCE was negligible for stoichiometric $TiO_2$ in the same region. As previously reported [43], these observations imply that the enhanced electron mobility and improved charge separation achieved via the introduction of oxygen vacancies mainly originate from the UV region.

The water splitting $H_2$ production, illustrated in Fig. 5 and Figs. S13 and S14 (in the ESM) was used to evaluate the photocatalytic activity of the $TiO_2$ NRs, B-$TiO_{2-x}$ NRs, S-$TiO_{2-x}$ NRs, and S-B-$TiO_{2-x}$ NRs. Under solar-light irradiation, the S-B-$TiO_{2-x}$ NRs (B-$TiO_{2-x}$ NRs (6 h) reduced for 5 min) steadily produced hydrogen gas at a rate of up to 106.98 μmol/h, which is notably higher than that of the B-$TiO_{2-x}$ NRs (56.58 μmol/h) and S-$TiO_{2-x}$ NRs (48.94 μmol/h) under the same conditions. The prepared rutile $TiO_2$ NRs are more active than the commercial $TiO_2$ NPs (8.49 μmol/h vs. minimal $H_2$ production). The samples prepared using different reaction times show different $H_2$ evolution rates where the maximum $H_2$ production rate was

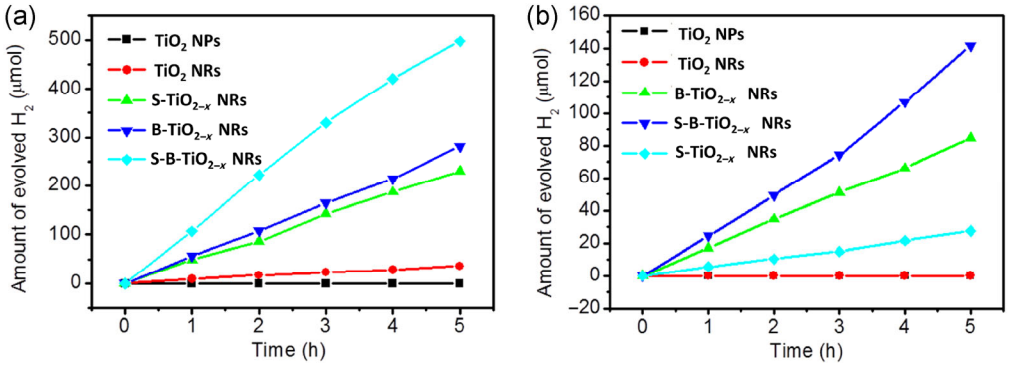


**Figure 5** Time courses of $H_2$ production from as-prepared samples loaded with 1% Pt in 30% methanol/water (a) under simulated sunlight and (b) under illumination with Xeon lamp (300 W) with UV-420 cut-off filter.

achieved at the mid-range of the reaction time. This indicates that an optimal concentration of oxygen vacancies exists for the different series of samples, as shown in Fig. S13 (in the ESM). The visible-light photocatalytic hydrogen generation performance is also shown in Figs. 5(b) and Fig. S14 (in the ESM), demonstrating trends similar to those of the samples measured under 300 W Xe lamp irradiation with an UV 420 cutoff optical filter ($\lambda > 420$ nm). The photocatalytic activity of the S-B-$TiO_{2-x}$ NRs remained unchanged after five cycles without any noticeable decrease, demonstrating the excellent stability of this sample (Fig. 6(a)). All these investigations demonstrate that the S-B-$TiO_{2-x}$ samples with oxygen vacancies present in the bulk and on the surface, prepared via the two-step reduction process, exhibited the best photocatalytic activity among the evaluated samples. Based on the above analysis, a possible mechanism may involve introduction of an inter-band-gap state by the oxygen vacancies, leading to the visible light response [8]. Furthermore, the oxygen vacancies served as shallow donors that may increase the carrier density and improve the electrical conductivity. The optimized oxygen vacancy concentration may also improve the separation and transfer properties of the charge carriers, as schematically illustrated in Fig. 6. However, excessive oxygen vacancies could serve as recombination centers, leading to decreased photocatalytic activity [44]. Although the current analytical technique is not effective for quantifying or identifying the distribution of oxygen vacancies, the present results show that optimization of the oxygen vacancies implanted in the bulk and on the sample surface may enhance the optical and electronic properties of metal oxide semiconductors.

## 4 Conclusions

In conclusion, we have developed a simple two-step approach for the production of controllable oxygen vacancies implanted on the surface or in the bulk of one-dimensional rutile $TiO_2$ NRs with defined facets. Self-doped $TiO_2$ NRs were synthesized via the

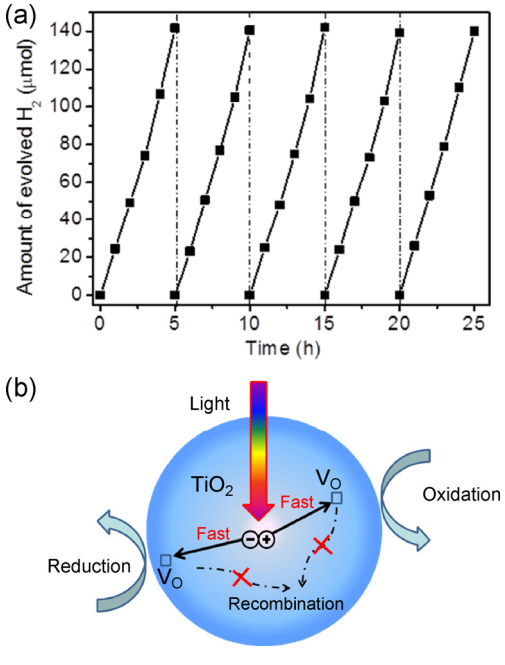


**Figure 6** (a) Evaluation of visible light-driven photocatalytic activity of S-B-$TiO_{2-x}$ NRs via cycling tests. (b) Illustration of oxygen vacancies that facilitate rapid charge transfer and separation.

hydrothermal route. Surface-implanted defects were subsequently introduced by subsequent solid-state reaction with $NaBH_4$. All $TiO_2$ samples containing oxygen vacancies exhibit remarkably higher photocatalytic performance than the original pristine $TiO_2$ NRs. The significantly improved photocatalytic activity and photocurrent response of the prepared samples can be attributed to the enhanced donor density, higher electronic conductivity, and improved charge separation, which is attributed to the introduction of oxygen vacancies by various defect-implantation methods. An optimum concentration of both bulk and surface introduced oxygen vacancies is required to maximize the improvement of the photocatalytic performance. This study should shed light on the future development of photocatalytic materials based on $TiO_2$.

## Acknowledgements

The authors thank the National Natural Science Foundation of China (Nos. 21301166, 21201159, 61361166004, and 61176016); Science and Technology Department of Jilin Province (No. 20130522127JH) are gratefully acknowledged. Z. C. S. thanks the support of the "Hundred Talent program" of CAS and open research fund program of State Key Laboratory of Luminescence and Applications (Changchun Institute of Optics, Fine Mechanics and Physics, CAS). Z. Z. thanks for the support of the fellowship from China Scholarship Council. Financial support of the project from the National Science Foundation (No. CHE-1213795, P. Y. F.) is also greatly appreciated.

**Electronic Supplementary Material**: Supplementary material (more SEM, optical images, XRD, $N_2$ absorb, and EPR, photocatalytic $H_2$ production) is available in the online version of this article at http://dx.doi.org/10.1007/s12274-015-0917-5.

## References

[1] Hoffmann, M. R.; Martin, S. T.; Choi, W.; Bahnemann, D. W. Environmental applications of semiconductor photocatalysis. *Chem. Rev.* **1995**, *95*, 69–96.

[2] Chen, X. B.; Shen, S. H.; Guo, L. J.; Mao, S. S. Semiconductor-based photocatalytic hydrogen generation. *Chem. Rev.* **2010**, *110*, 6503–6570.

[3] Bard, A. J.; Fox, M. A. Artificial photosynthesis: Solar splitting of water to hydrogen and oxygen. *Acc. Chem. Res.* **1995**, *28*, 141–145.

[4] Li, X.; Wen, J. Q.; Low, J.; Fang, Y. P.; Yu, J. G. Design and fabrication of semiconductor photocatalyst for photocatalytic reduction of $CO_2$ to solar fuel. *Sci. China Mater.* **2014**, *57*, 70–100.

[5] Ma, Y.; Wang, X. L.; Jia, Y. S.; Chen, X. B.; Han, H. X.; Li, C. Titanium dioxide-based nanomaterials for photocatalytic fuel generations. *Chem. Rev.* **2014**, *114*, 9987–10043.

[6] Liu, L.; Chen, X. B. Titanium dioxide nanomaterials: Self-structural modifications. *Chem. Rev.* **2014**, *114*, 9890–9918.

[7] Bally, A. R.; Korobeinikova, E. N.; Schmid, P. E.; Lévy, F.; Bussy, F. Structural and electrical properties of Fe-doped $TiO_2$ thin films. *J. Phys. D: Appl. Phys.* **1998**, *31*, 1149–1154.

[8] Nowotny, M. K.; Sheppard, L. R.; Bak, T.; Nowotny, J. Defect chemistry of titanium dioxide. Application of defect engineering in processing of $TiO_2$-based photocatalysts. *J. Phys. Chem. C* **2008**, *112*, 5275–5300.

[9] Pan, X. Y.; Yang, M. Q.; Fu, X. Z.; Zhang, N.; Xu, Y. J. Defective $TiO_2$ with oxygen vacancies: Synthesis, properties and photocatalytic applications. *Nanoscale* **2013**, *5*, 3601–3614.

[10] Hu, Y. H. A highly efficient photocatalyst - Hydrogenated black $TiO_2$ for the photocatalytic splitting of water. *Angew. Chem., Int. Ed.* **2012**, *51*, 12410–12412.

[11] Naldoni, A.; Allieta, M.; Santangelo, S.; Marelli, M.; Fabbri, F.; Cappelli, S.; Bianchi, C. L.; Psaro, R.; Dal Santo, V. Effect of nature and location of defects on bandgap narrowing in black $TiO_2$ nanoparticles. *J. Am. Chem. Soc.* **2012**, *134*, 7600–7603.

[12] Zuo, F.; Wang, L.; Wu, T.; Zhang, Z. Y.; Borchardt, D.; Feng, P. Y. Self-doped $Ti^{3+}$ enhanced photocatalyst for hydrogen production under visible light. *J. Am. Chem. Soc.* **2010**, *132*, 11856–11857.

[13] Zheng, Z. K.; Huang, B. B.; Meng, X. D.; Wang, J. P.; Wang, S. Y.; Lou, Z. Z.; Wang, Z. Y.; Qin, X. Y.; Zhang, X. Y.; Dai, Y. Metallic zinc-assisted synthesis of $Ti^{3+}$ self-doped $TiO_2$ with tunable phase composition and visible-light photocatalytic activity. *Chem. Commun.* **2013**, *49*, 868–870.

[14] Zhao, Z.; Tan, H. Q.; Zhao, H. F.; Lv, Y.; Zhou, L.-J.; Song, Y. J.; Sun, Z. C. Reduced $TiO_2$ rutile nanorods with well-defined facets and their visible-light photocatalytic activity. *Chem. Commun.* **2014**, *50*, 2755–2757.

[15] Zuo, F.; Bozhilov, K.; Dillon, R. J.; Wang, L.; Smith, P.; Zhao, X.; Bardeen, C.; Feng, P. Y. Active facets on titanium(III)-doped $TiO_2$: An effective strategy to improve the visible-light photocatalytic activity. *Angew. Chem., Int. Ed.* **2012**, *124*, 6327–6330.

[16] Justicia, I.; Ordejón, P.; Canto, G.; Mozos, J. L.; Fraxedas, J.; Battiston, G. A.; Gerbasi, R.; Figueras, A. Designed self-doped titanium oxide thin films for efficient visible-light photocatalysis. *Adv. Mater.* **2002**, *14*, 1399–1402.

[17] Han, B.; Hu, Y. H. Highly efficient temperature-induced visible light photocatalytic hydrogen production from water. *J. Phys. Chem. C* **2015**, *119*, 18927–18934.

[18] Wang, G. M.; Ling, Y. C.; Li, Y. Oxygen-deficient metal oxide nanostructures for photoelectrochemical water oxidation and other applications. *Nanoscale* **2012**, *4*, 6682–6691.

[19] Yang, Y.; Ling, Y. C.; Wang, G. M.; Li, Y. The effect of the hydrogenation temperature on $TiO_2$ nanostructures for photoelectrochemical water oxidation. *Eur. J. Inorg. Chem.* **2014**, *2014*, 760–766.

[20] Pesci, F. M.; Wang, G. M.; Klug, D. R.; Li, Y.; Cowan, A. J. Efficient suppression of electron–hole recombination in oxygen-deficient hydrogen-treated $TiO_2$ nanowires for photoelectrochemical water splitting. *J. Phys. Chem. C* **2013**, *117*, 25837–25844.

[21] Tan, H. Q.; Zhao, Z.; Niu, M.; Mao, C. Y.; Cao, D. P.; Cheng, D. J.; Feng, P. Y.; Sun, Z. C. A facile and versatile method for preparation of colored $TiO_2$ with enhanced solar-driven photocatalytic activity. *Nanoscale* **2014**, *6*, 10216–10223.

[22] Mao, C. Y.; Zuo, F.; Hou, Y.; Bu, X. H.; Feng, P. Y. *In situ* preparation of a $Ti^{3+}$ self-doped $TiO_2$ film with enhanced activity as photoanode by $N_2H_4$ reduction. *Angew. Chem., Int. Ed.* **2014**, *126*, 10653–10657.

[23] Zuo, F.; Bozhilov, K.; Dillon, R. J.; Wang, L.; Smith, P.; Zhao, X.; Bardeen, C.; Feng, P. Y. Active facets on titanium(III)-doped $TiO_2$: An effective strategy to improve the visible-light photocatalytic activity. *Angew. Chem., Int. Ed.* **2012**, *51*, 6223–6226.

[24] Xia, T.; Chen, X. B. Revealing the structural properties of hydrogenated black $TiO_2$ nanocrystals. *J. Mater. Chem. A* **2013**, *1*, 2983–2989.

[25] Zhou, W.; Li, W.; Wang, J.-Q.; Qu, Y.; Yang, Y.; Xie, Y.; Zhang, K. F.; Wang, L.; Fu, H. G.; Zhao, D. Y. Ordered mesoporous black $TiO_2$ as highly efficient hydrogen evolution photocatalyst. *J. Am. Chem. Soc.* **2014**, *136*, 9280–9283.

[26] Horikoshi, S.; Minatodani, Y.; Tsutsumi, H.; Uchida, H.; Abe, M.; Serpone, N. Influence of lattice distortion and oxygen vacancies on the UV-driven/microwave-assisted $TiO_2$ photocatalysis. *J. Photoch. Photobio. A* **2013**, *265*, 20–28.

[27] Diebold, U. The surface science of titanium dioxide. *Surf. Sci. Rep.* **2003**, *48*, 53–229.

[28] Li, X.; Yu, J. G.; Low, J.; Fang, Y. P.; Xiao, J.; Chen, X. B. Engineering heterogeneous semiconductors for solar water splitting. *J. Mater. Chem. A* **2015**, *3*, 2485–2534.

[29] Chen, X. B.; Liu, L.; Huang, F. Q. Black titanium dioxide ($TiO_2$) nanomaterials. *Chem. Soc. Rev.* **2015**, *44*, 1861–1885.

[30] Chen, X. B.; Liu, L.; Liu, Z.; Marcus, M. A.; Wang, W.-C.; Oyler, N. A.; Grass, M. E.; Mao, B. H.; Glans, P.-A.; Yu, P. Y. et al. Properties of disorder-engineered black titanium dioxide nanoparticles through hydrogenation. *Sci. Rep.* **2013**, *3*, 1510.

[31] Hamdy, M. S.; Amrollahi, R.; Mul, G. Surface $Ti^{3+}$-containing (blue) titania: A unique photocatalyst with high activity and selectivity in visible light-stimulated selective oxidation. *ACS. Catal.* **2012**, *2*, 2641–2647.

[32] Hanawa, T. A comprehensive review of techniques for biofunctionalization of titanium. *J. Periodontal Implant Sci.* **2011**, *41*, 263–272.

[33] Conesa, J. C.; Soria, J. Reversible titanium(3+) formation by hydrogen adsorption on m/anatase ($TiO_2$) catalysts. *J. Phys. Chem.* **1982**, *86*, 1392–1395.

[34] Zuo, F.; Wang, L.; Feng, P. Y. Self-doped $Ti^{3+}$@$TiO_2$ visible light photocatalyst: Influence of synthetic parameters on the $H_2$ production activity. *Int. J. Hydrogen Energy* **2014**, *39*, 711–717.

[35] Sayed, F. N.; Jayakumar, O. D.; Sasikala, R.; Kadam, R. M.; Bharadwaj, S. R.; Kienle, L.; Schürmann, U.; Kaps, S.; Adelung, R.; Mittal, J. P. et al. Photochemical hydrogen generation using nitrogen-doped $TiO_2$–Pd nanoparticles: Facile synthesis and effect of $Ti^{3+}$ incorporation. *J. Phys. Chem. C* **2012**, *116*, 12462–12467.

[36] Howe, R. F.; Gratzel, M. EPR Observation of trapped electrons in colloidal titanium dioxide. *J. Phys. Chem.* **1985**, *89*, 4495–4499.

[37] Lu, H. Q.; Zhao, B. B.; Pan, R. L.; Yao, J. F.; Qiu, J. H.; Luo, L.; Liu, Y. C. Safe and facile hydrogenation of commercial degussa P25 at room temperature with enhanced photocatalytic activity. *RSC Adv.* **2014**, *4*, 1128–1132.

[38] Teng, F.; Li, M. Y.; Gao, C. T.; Zhang, G. Z.; Zhang, P.; Wang, Y. Q.; Chen, L. L.; Xie, E. Q. Preparation of black $TiO_2$ by hydrogen plasma assisted chemical vapor deposition and its photocatalytic activity. *Appl. Catal. B-Environ.* **2014**, *148–149*, 339–343.

[39] Maeda, Y.; Iizuka, Y.; Kohyama, M. Generation of oxygen vacancies at a Au/$TiO_2$ perimeter interface during CO oxidation detected by *in situ* electrical conductance

measurement. *J. Am. Chem. Soc.* **2013**, *135*, 906–909.

[40] Strunk, J.; Vining, W. C.; Bell, A. T. A study of oxygen vacancy formation and annihilation in submonolayer coverages of $TiO_2$ dispersed on MCM-48. *J. Phys. Chem. C* **2010**, *114*, 16937–16945.

[41] Yu, X. M.; Kim, B.; Kim, Y. K. Highly enhanced photoactivity of anatase $TiO_2$ nanocrystals by controlled hydrogenation-induced surface defects. *ACS. Catal.* **2013**, *3*, 2479–2486.

[42] Maeda, K.; Higashi, M.; Siritanaratkul, B.; Abe, R.; Domen, K. $SrNbO_2N$ as a water-splitting photoanode with a wide visible-light absorption band. *J. Am. Chem. Soc.* **2011**, *133*, 12334–12337.

[43] Wang, G. M.; Wang, H. Y.; Ling, Y. C.; Tang, Y. C.; Yang, X. Y.; Fitzmorris, R. C.; Wang, C. C.; Zhang, J. Z.; Li, Y. Hydrogen-treated $TiO_2$ nanowire arrays for photoelectrochemical water splitting. *Nano Lett.* **2011**, *11*, 3026–3033.

[44] Ling, Y. C.; Wang, G. M.; Reddy, J.; Wang, C. C.; Zhang, J. Z.; Li, Y. The influence of oxygen content on the thermal activation of hematite nanowires. *Angew. Chem., Int. Ed.* **2012**, *124*, 4150–4155.